A depth-of-interaction PET detector using a stair-shaped reflector arrangement and a single-ended scintillation light readout

2017 Phys. Med. Biol. 62 465

(http://iopscience.iop.org/0031-9155/62/2/465)

IOP Publishing | Institute of Physics and Engineering in Medicine Physics in Medicine & Biology

Phys. Med. Biol. **62** (2017) 465–483 doi:10.1088/1361-6560/aa5076

A depth-of-interaction PET detector using a stair-shaped reflector arrangement and a single-ended scintillation light readout

Jeong-Whan Son[1,2], Min Sun Lee[1,3] and Jae Sung Lee[1,2,3,4,5]

[1] Department of Nuclear Medicine, Seoul National University College of Medicine, Seoul 110-744, Korea
[2] Department of Biomedical Sciences, Seoul National University College of Medicine, Seoul 110-744, Korea
[3] Interdisciplinary Programs in Radiation Applied Life Science, Seoul National University, Seoul 110-744, Korea
[4] Institute of Radiation Medicine, Medical Research Center, Seoul National University College of Medicine, Seoul 110-744, Korea

E-mail: jaes@snu.ac.kr

Received 15 September 2016, revised 3 November 2016
Accepted for publication 29 November 2016
Published 21 December 2016

Abstract

Positron emission tomography (PET) detectors with the ability to encode depth-of-interaction (DOI) information allow us to simultaneously improve the spatial resolution and sensitivity of PET scanners. In this study, we propose a DOI PET detector based on a stair-pattern reflector arrangement inserted between pixelated crystals and a single-ended scintillation light readout. The main advantage of the proposed method is its simplicity; DOI information is decoded from a flood map and the data can be simply acquired by using a single-ended readout system. Another potential advantage is that the two-step DOI detectors can provide the largest peak position distance in a flood map because two-dimensional peak positions can be evenly distributed. We conducted a Monte Carlo simulation and obtained flood maps. Then, we conducted experimental studies using two-step DOI arrays of 5×5 $Lu_{1.9}Y_{0.1}SiO_5$:Ce crystals with a cross-section of $1.7 \times 1.7\,mm^2$ and different detector configurations: an unpolished single-layer ($_US$) array, a polished single-layer ($_PS$) array and a polished stacked two-layer ($_PT$) array. For each detector configuration, both air gaps and room-temperature vulcanization (RTV) silicone gaps were tested. Detectors $_US$ and $_PT$ showed good peak separation in each scintillator with an average peak-to-valley ratio (PVR)

[5] Author to whom any correspondence should be addressed.
Department of Nuclear Medicine, Seoul National University College of Medicine, 103 Daehak-ro, Jongno-gu, Seoul 110-744, Korea.

and distance-to-width ratio (DWR) of 2.09 and 1.53, respectively. Detector ${}_{P}S_{RTV}$ showed lower PVR and DWR (1.65 and 1.34, respectively). The configuration of detector ${}_{P}T_{Air}$ is preferable for the construction of time-of-flight-DOI detectors because timing resolution was degraded by only about 40 ps compared with that of a non-DOI detector. The performance of detectors ${}_{U}S_{Air}$ and ${}_{P}S_{RTV}$ was lower than that of a non-DOI detector, and thus these designs are favorable when the manufacturing cost is more important than timing performance. The results demonstrate that the proposed DOI-encoding method is a promising candidate for PET scanners that require high resolution and sensitivity and operate with conventional acquisition systems.

Keywords: positron emission tomography, depth of interaction, single-ended readout, light sharing

(Some figures may appear in colour only in the online journal)

1. Introduction

Positron emission tomography (PET) is a powerful *in vivo* molecular imaging modality used for clinical and research purposes (Troost *et al* 2010, Lee and Park 2014, Lee *et al* 2015, Yoo *et al* 2015). Advanced PET systems require detector modules with excellent intrinsic detector performance. Recent advances in the development of scintillation crystals and semiconductor photosensors have led to a remarkable improvement of PET detector technologies (e.g. Kwon *et al* 2011, Yoon *et al* 2012, Ko *et al* 2016). For example, PET detectors based on cerium-doped lutetium silicate scintillators and silicon photomultipliers (SiPMs) yield excellent timing resolution, which is required for time-of-flight (TOF) measurements in clinical whole-body PET systems (Cates and Levin 2016). The small pixel size (<6 mm) and narrow gap between each pixel (<0.5 mm) of multi-anode metal-package photomultiplier tubes (PMTs) and SiPM arrays provide the high spatial resolution (Yamamoto *et al* 2013, Ko and Lee 2015) compared with conventional block detectors consisting of an array of single-anode PMTs, because the former have a higher coupling ratio of photosensor pixels to scintillation crystals. Good spatial resolution is required in PET detectors for resolving small crystal elements used in small-animal-dedicated or human-organ-specific PET scanners.

PET detectors with the capability of encoding depth-of-interaction (DOI) information improve the spatial resolution in the peripheral field of view of small-ring PET scanners by reducing the parallax error (Yamaya *et al* 2006). Measurement of DOI is also preferred in PET scanners with a relatively long axial length because it is useful for mitigating the degradation of axial resolution due to mispositioning of oblique lines of response (Yu *et al* 2014). Moreover, the combination of DOI and TOF technologies for the further reduction of the positional uncertainty of annihilation photon pair generation is a currently an active research topic (Kang *et al* 2015, Berg *et al* 2016). This synergy is expected to be beneficial, because DOI information is also useful for correcting for the depth-dependent time walk of the scintillation pulses that degrades the timing resolution (Ito *et al* 2011, Spanoudaki and Levin 2011).

Many innovative methods have been suggested for DOI measurements in PET detectors and all have advantages and disadvantages. Two widely used approaches are pulse-shape analysis using scintillation crystals with different decay times and a relative offset method based on stacking two or four crystal arrays with a relative offset (Seidel *et al* 1999, Liu *et al* 2001, Zhang *et al* 2002, Ito *et al* 2010a). However, in the pulse-shape analysis method, the use of crystals with different decay times leads to an increase in the material cost because one of the

two crystals is usually not a common one. The relative offset method requires accurate and precise alignment of the stacked crystal arrays. Excellent DOI resolution can be achieved by the dual-ended readout of the scintillation light emitted from continuous pixelated crystals (e.g. Delfino *et al* 2010, Kang *et al* 2015); however, the increase in cost due to the two-fold increase in the number of photosensors required compared with conventional single-ended readout is a disadvantage of this approach.

DOI measurement in a monolithic crystal detector employing a continuous crystal slab is also an active research area because monolithic crystal detectors are cost-effective and offer a higher packing fraction than pixelated ones (Ling *et al* 2007, Maas *et al* 2009, Chung *et al* 2010). Because DOI measurement in monolithic crystal relies on a wide light dispersion pattern, this approach has limited performance at the edge of a crystal slab. In addition, there is a tradeoff between DOI and positional accuracy and crystal thickness. An approach free from this tradeoff is the measurement of DOI by tailoring the light spreading pattern using triangular light reflectors inserted between pixelated crystals (Ito *et al* 2010b, Ito *et al* 2013, Lee and Lee 2015), because specially arranged reflectors can alter the pattern of scintillation light dispersion (Marcinkowski *et al* 2014, Streun *et al* 2014). This method requires only a single-layer pixelated crystal array and a single-ended readout for obtaining continuous DOI information with a DOI resolution of 4.2 mm from 20 mm scintillators; however, this technique needs the readout of the row and column sums of the individual output signals from the photosensor array to estimate the DOI position from the light-spreading pattern.

In this study, we propose a new DOI-encoding method that employs stair-pattern reflectors inserted between pixelated crystals in a scintillation crystal array for two-step discrete DOI encoding (i.e. a 10 mm DOI resolution if 20 mm scintillators are used). The main advantage of this method is its simplicity because it requires only:

- a single-ended readout of the scintillation light
- DOI decoding from the flood map of the crystal array
- moderate assembly time and skill

Because the DOI position is determined from the flood map of the crystals (similarly to the relative offset method), only the readouts of four position-related signals are necessary if we use a charge-division network circuit to obtain the flood map (Siegel *et al* 1996). Here, we present the design concept of this approach and describe Monte Carlo simulations and experimental studies performed to demonstrate the feasibility of this new method. The impact of the crystal surface conditions (i.e. polished or unpolished), the DOI configurations (i.e. single-layer crystals or two-layer staggered crystals) and the gap materials (i.e. air or optical grease) between crystals on detector performance and pixel coding efficiency (PCE) on the flood map was explored. We have focused on the qualitative (i.e. peak-to-valley ratio (PVR) and distance-to-width ratio (DWR)) and quantitative (i.e. accuracy of DOI identification) measurement of PCE because it is one of the main factors determining the PET image quality of DOI PET (Stonger and Johnson 2004, Schellenberg *et al* 2016).

2. Materials and methods

2.1. Design concept

Most of the conventional PET detectors without DOI-encoding capability consist of a single-layer array of scintillation crystals coupled with the array of photosensors. Sometimes, position-sensitive photosensors, such as multi-channel PMTs and position-sensitive avalanche photodiodes, are used instead of a photosensor array (Dokhale *et al* 2004, Tashima *et al* 2016).

The electric signal outputs from the photosensors are multiplexed to reduce the number of output channels by using Anger-like logic, row/column sum circuits or charge division networks (Siegel *et al* 1996, Karp *et al* 2003, Kwon and Lee 2014). The multiplexed signals are recorded using charge-measurement devices such as analog to digital converters (ADCs), and the position of the gamma-ray interaction in the crystal array is decoded from the flood map (i.e. a two-dimensional (2D) histogram of the gamma-ray interaction positions) using the corresponding decoding equations for each multiplexing method. Basically, the gamma-ray interaction position (X and Y coordinates) for each event is determined by the weighted mean of the readout signals. The peak positions shown in the flood map correspond to the positions of the crystals in the array.

In these conventional PET detectors, each crystal element in the array is surrounded by light reflectors, such as thread seal tape (also known as Teflon tape) or 3M enhanced specular reflectors (ESR), to enhance the crystal identification in the flood map. These reflectors increase the distance between the peak positions and reduce the dispersion of the interaction positions in the flood map. Sometimes, shorter reflectors are placed at the center of the crystal array to make the distances between the crystals more uniform (Wong *et al* 2015).

By modifying the shape and arrangement of the reflectors, we can move the peak positions in the flood map (Murayama *et al* 1998, Tsuda *et al* 2004, Inadama *et al* 2008). For instance, if we remove the reflector between two crystals, the peak position is shifted toward their mid-distance. Thus, the stair-shaped arrangement of reflectors shown in figures 1(b) and (c) lead to a shift of the peak positions in diagonal directions. By applying the reflector arrangement shown in figure 1(b) to the upper segment of the crystal array and that displayed in figure 1(c) to the lower segment, as shown in figure 1(a), we can decode two different DOI positions (upper or lower) in the flood map, as shown in figure 1(d). The ideal situation in this DOI-encoding method is that the shifted peak positions are evenly distributed on the straight diagonal lines in the flood map, as shown in figure 1(d).

2.2. Monte Carlo simulation

Prior to the experiment, a Monte Carlo simulation study was conducted as a proof of concept of our proposed two-step DOI detector. The GATE v.7.0 Monte Carlo simulation toolkit (Jan *et al* 2004) was used for generation and tracking of individual optical photons. The UNIFIED model (Levin and Moisan 1996) was employed to simulate photon interactions at medium boundaries. For the DOI detector, the crystal array consisted of 9×9 LSO (Lu_2SiO_5; 7.4 g cm^{-3}) crystal elements with cross sections of 1.7×1.7 mm^2. The height of the array was 20 mm for both the single-layer and two-layer stacked crystals. The refractive index of the LSO crystal was set to 1.82 and the light yield to 26 000 photons MeV^{-1}. Stair-shaped reflector polymers with specular type reflectivity (98%) and a thickness of 0.065 mm were inserted between the crystals, as shown in figure 2(a). The heights of the upper and lower segments of the scintillators (8 and 12 mm, respectively) were determined based on an additional simulation with the condition that both layers yield similar numbers of gamma-ray interactions. The two-step DOI scintillator array was coupled to a multi-anode PMT, which was modeled to contain 16×16 anodes of size 2.8×2.8 mm^2 and a pitch of 3.04 mm. Figure 2(b) shows the arrangement of the PMT pixels and the two-step DOI scintillator array. The PMT entrance window (glass, 2.5 g cm^{-3}) was set to be 1.5 mm thick and its refractive index was 1.50. A 0.1 mm thick optical adhesive ($C_1H_1O_1$, 1.0 g cm^{-3}) with refractive index 1.465 was inserted between the crystal array and the PMT.

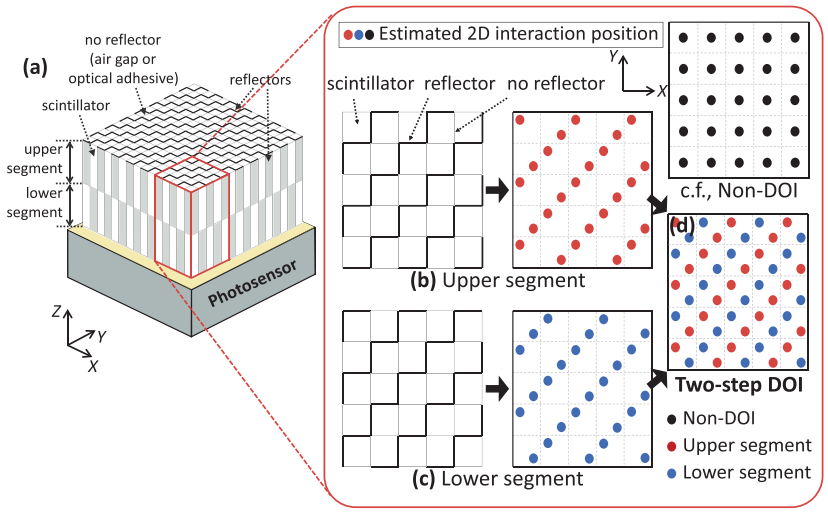

Figure 1. (a) Two-step DOI detector using a stair-shaped reflector arrangement with a relative offset of one crystal pitch in both *X* and *Y* directions between the upper and lower segments. The corresponding flood maps of 5 × 5 scintillators of (b) the upper and (c) the lower segment. (d) DOI information can be decoded from the flood map of the detector.

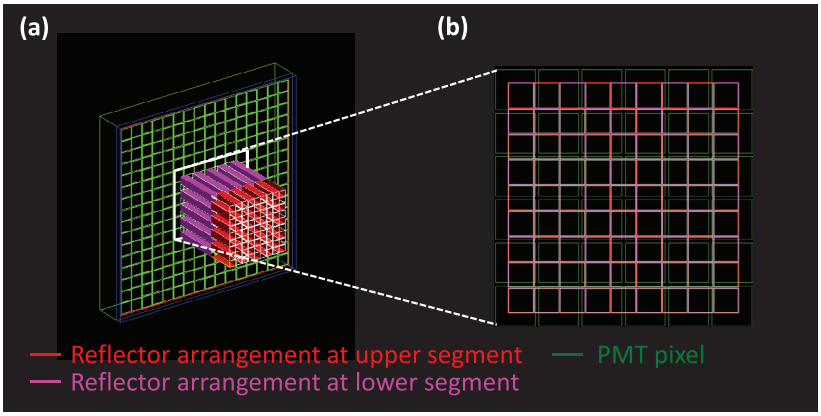

Figure 2. A Monte Carlo simulation setup. (a) The two-step DOI detector of 9 × 9 single-layer unpolished scintillators and (b) the arrangement of the scintillators on the pixels of a photosensor.

To characterize the proposed DOI detector, six detector configurations were tested by changing the crystal surface conditions (i.e. polished or unpolished), the DOI configurations (i.e. single-layer crystals or two-layer staggered crystals) and the gap materials (i.e. air or optical adhesive) between crystals. The configurations, which have different light dispersions in the crystal array, were as follows: unpolished single-layer crystals with (1) air gaps and (2) optical adhesive gaps, polished single-layer crystals with (3) air gaps and (4) optical adhesive gaps, and polished two-layer stacked crystals with (5) air gaps and (6) optical adhesive gaps.

The effect of different types of reflectors (i.e. specular or diffusive) on DOI performance was not tested because similar results were obtained. Optical adhesive was inserted between the pixelated crystals to enhance the probability of light transmission and to increase the distance between the peak positions (Nishikido *et al* 2014). Inserting optical adhesive having a similar refractive index to that of scintillation crystals increases the critical angle so that more scintillation photons can be spread to the adjacent crystals which would otherwise be reflected back. The top face (the opposite face of the surface contacting the entrance window of the photosensors) and four outermost faces of the scintillator blocks were covered by reflectors to maximize the collection of scintillation light.

The crystal surface and medium boundaries were simulated using the 'ground model', which is based on the UNIFIED model, by specifying the standard deviation (sigma-alpha, σ_α) of the Gaussian distribution of micro-facets around the average surface normal. We used a sigma-alpha value of 5.6 for the unpolished crystal surface and 0.1 for the polished crystal surface, which were directly measured by scanning the crystal surface using atomic force microscopy (Ito *et al* 2010b). The photon interactions at the medium boundaries were simulated based on user-defined surface conditions and the refractive indices or reflectivity. The simulated photons were detected in the PMT pixels. Approximately 200 000 events were acquired from the simulation, and flood histograms were generated for six detector configurations based on the PMT pixel outputs to determine the DOI-encoding capability. In this study, we did not consider any electronic and PMT noises or any crystal light yields.

2.3. Detector block and experimental setup

2.3.1. Detector block. The two-step DOI scintillator arrays were assembled using 5 × 5 LYSO crystals ($Lu_{1.9}Y_{0.1}SiO_5$:Ce; Epic Crystal Co., China) with a cross section of 1.7 × 1.7 mm^2 and a 0.1 mm gap between crystals. The size of the arrays was 9.1 × 9.1 × 20 mm^3. To achieve two-step DOI encoding, the height of the upper segment was 8 mm and that of the lower segment 12 mm, as determined in the simulation study. The ESRs (3M, USA) were folded to form a stair-like shape and inserted between the crystals as reflective materials. To investigate the feasibility of the DOI-encoding method for different crystal surface treatments and DOI configurations, six different detectors were fabricated: two unpolished single-layer LYSO arrays, one with air gaps (detector $_{U}S_{Air}$) and one with room-temperature vulcanization (RTV) silicone (refractive index 1.45; KE420, Shin-Etsu Chemical Co., Ltd, Japan) gaps (detector $_{U}S_{RTV}$), two polished single-layer LYSO arrays, one with air gaps (detector $_{P}S_{Air}$) and one with RTV silicone gaps (detector $_{P}S_{RTV}$), and two polished two-layer stacked LYSO arrays, one with air gaps (detector $_{P}T_{Air}$) and one with RTV silicone gaps (detector $_{P}T_{RTV}$), as shown in figure 3. RTV silicone was implemented to enhance the light transmission between adjacent scintillators, as described in section 2.2. The unpolished crystals were lapped with a 1200-grit polishing kit except on the surfaces with a 1.7 × 1.7 mm^2 cross section. For detectors $_{P}T_{Air}$ and $_{P}T_{RTV}$, the upper and lower layers were coupled using optical grease (BC-630, OKEN, Japan). In all DOI scintillator arrays, the outermost surfaces—except the surface contacting the photosensor—were covered by reflectors to enhance the detection efficiency of the edge crystals for scintillation light. The configurations of the six detectors are summarized in table 1.

2.3.2. Experimental setup.

2.3.2.1. Gamma-ray irradiation scheme. The front surfaces of the DOI detectors were irradiated with gamma rays (i.e. front-on irradiation) to obtain the flood histograms and analyze the DOI identification accuracy; irradiation of their side surfaces (i.e. side-on irradiation) was also conducted to evaluate the energy and timing performance of each segment. In the side-on

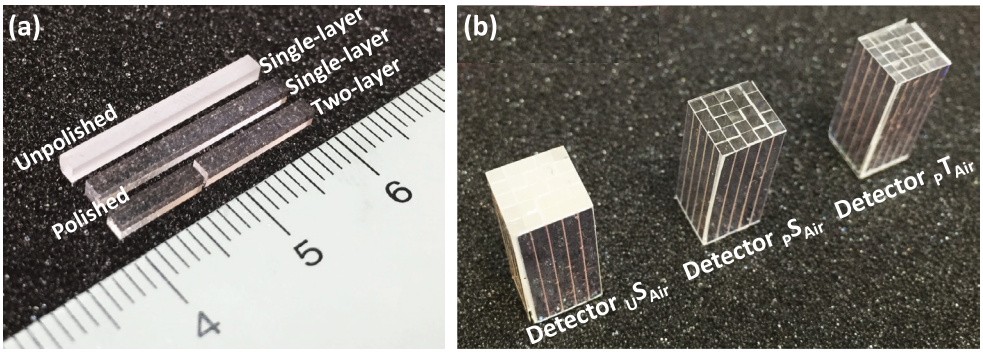

Figure 3. Scintillators and DOI detectors used in the experimental studies. (a) An unpolished single-layer LYSO array (20 mm long), a polished single-layer LYSO (20 mm long) array and a polished two-layer stacked LYSO (8 mm and 12 mm long each) array. (b) Two-step DOI detectors with air gaps based on different crystal surface treatments and DOI configurations using the LYSO array shown in (a).

Table 1. Summary of the six detector configurations and the reference detector.

Detector	$_{U}S_{Air}$	$_{U}S_{RTV}$	$_{P}S_{Air}$	$_{P}S_{RTV}$	$_{P}T_{Air}$	$_{P}T_{RTV}$	REF
Scintillator surface treatment	Unpolished		Polished		Polished		Polished
DOI block configuration	Single-layer		Single-layer		Two-layer		Single-layer
Gap material	Air	RTV	Air	RTV	Air	RTV	ESR
DOI capability	Two-step		Two-step		Two-step		None

irradiation schemes, the center of each segment (i.e. 4 mm from the top face for the upper segment and 6 mm from the bottom face for the lower segment) was irradiated. As a reference, side-on irradiation data were also acquired for a non-DOI array of polished single-layer 5 × 5 LYSO scintillators (detector REF). For the side-on irradiation, depth-dependent data acquisition (DAQ) was performed by shielding the other segment with a lead block.

2.3.2.2. Detector module and DAQ setup. The DOI scintillator arrays were coupled with a multi-channel PMT (H9500, Hamamatsu Photonics K. K., Japan) using optical grease. The H9500 PMT had a 16 × 16 array of anodes with an anode size 2.8 × 2.8 mm^2 and a gap of 0.24 mm between anodes. The H9500 PMT was chosen because of its smaller pixel size (i.e. 2.8 mm) compared with those (i.e. 5.8 mm or 6 mm) of other multi-anode PMTs (i.e. H8500 or H12700, respectively) having an 8 × 8 array of anodes. The H9500 PMT was expected to be beneficial for resolving scintillators with a small cross-section as well as 2D light distribution estimations, thus improving DOI resolution. The front-end electronics included an anode gain compensator (Lee *et al* 2012), a resistive positioning circuit (Kwon *et al* 2008) and amplifiers. Trigger signals were generated from the dynode signals using a fast amplifier circuit (Son *et al* 2016). To acquire coincidence data, a reference single-channel PMT (R9800, Hamamatsu Photonics K. K., Japan) coupled with a LYSO scintillator (4 × 4 × 10 mm^3) was used. A ^{22}Na point source (25 μCi, 0.25 mm diameter; MMS06-022, Eckert & Ziegler, Germany) was attached on the front of the reference detector. The distance between the DOI detector and the reference detector was 8 cm. The trigger signals from both detectors were transferred to a field-programmable gate array (FPGA)-based time-to-digital converter (Won *et al* 2016)

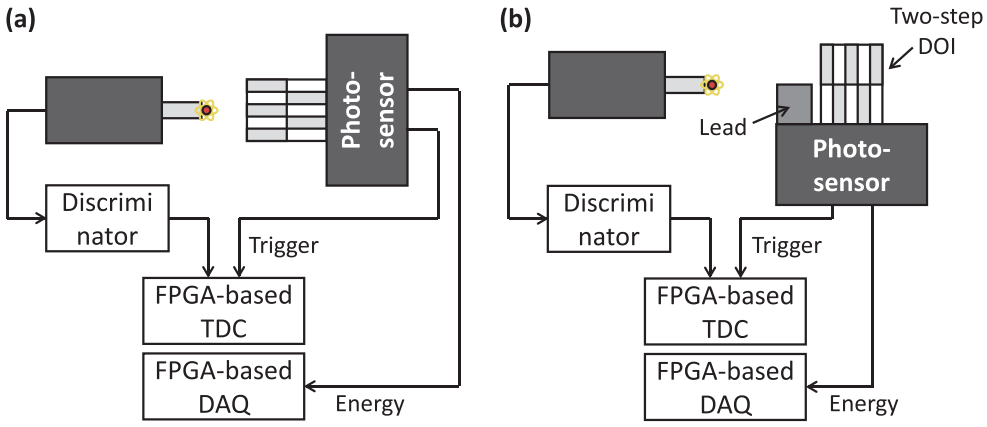

Figure 4. The experimental setup and the data acquisition system. (a) The front surfaces of the DOI detectors were irradiated with gamma rays to obtain the flood maps and analyze the accuracy of DOI identification. (b) The side surfaces of the DOI detectors were irradiated to evaluate the energy and timing performance. A custom-built FPGA-based time-to-digital converter and data acquisition system were used.

to obtain the arrival time information. The position-encoding signals were digitized using free-running ADCs and were integrated to obtain energy information using a FPGA-based DAQ system (Yoon 2016). The DAQ system synchronized the time and energy information and transferred the data to a personal computer. Figure 4 shows diagrams of the experimental setup.

2.4. Data analysis

2.4.1. DOI identification accuracy. Flood histograms were generated from the front-on irradiation data using events with energies higher than 400 keV. In the flood maps, the accuracy of the separation between two peak positions in one crystal (i.e. the accuracy of the DOI identification) was evaluated using parameters such as the PVR and the DWR. Both parameters were calculated from the 1D profile obtained along the line connecting two peak positions in each crystal, as shown in figure 5. From the profile, the PVR was determined as the average ratio of the counts measured in the two peaks to those in a valley. The average PVR of a DOI scintillator array was calculated with the following equation:

$$\mathrm{PVR}_{\mathrm{avg}} = \frac{1}{N}\sum_{i=1}^{N}\left(\left(\frac{Y_{\mathrm{p1}}}{Y_{\mathrm{v}}} + \frac{Y_{\mathrm{p2}}}{Y_{\mathrm{v}}}\right)/2\right)$$

where N is the number of examined scintillation crystals in a detector and p1 and p2 are the indices for the two peaks in a crystal. The DWR was determined as the ratio of the distance between the two peaks to the average full-width at half-maximum (FWHM) of the two peak distributions. The average DWR of a DOI array was calculated as follows:

$$\mathrm{DWR}_{\mathrm{avg}} = \frac{1}{N}\sum_{i=1}^{N}\left(\frac{\left|X_{\mathrm{p1}} - X_{\mathrm{p2}}\right|}{(\mathrm{FWHM}_{\mathrm{p1}} + \mathrm{FWHM}_{\mathrm{p2}})/2}\right).$$

We calculated the accuracy of DOI identification also based on the 1D profile across two peaks. After eliminating the background counts due to intercrystal scattering by a tail fitting

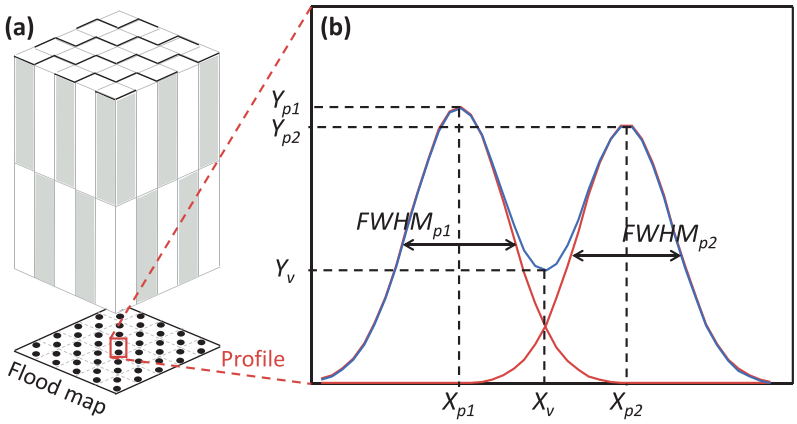

Figure 5. (a) A two-step DOI detector and the corresponding flood map. (b) The 1D profile of the two peaks in one scintillator. The PVR and the DWR were calculated from the profile.

method, the Gaussian mixture model was applied to the profile to estimate two separate Gaussian distributions around the peaks. Then, in each Gaussian distribution, the areas under the curve (AUC) split by the crossing point (i.e. X_V in figure 5(b)) of two Gaussian distributions were calculated respectively. Finally, the accuracy of DOI identification was obtained by the percentage ratio of the AUC in the peak side and the total AUC.

Among the 5 × 5 scintillators, only the central 3 × 3 crystals were analyzed to derive the DOI identification accuracy because of the limited shift of the peak position in the crystals located in the edge and corner regions.

2.4.2. Energy performance. Energy spectra were generated from the side-on irradiation data and the energy peak and resolution were obtained for each segment of each crystal. The energy resolution was calculated as the FWHM of a Gaussian function fitted to the 511 keV photopeak normalized by the peak. The energy results from the upper and lower segments were compared to determine the depth-dependent energy performance.

2.4.3. Time performance. Histograms of the arrival time difference were obtained from the side-on irradiation data with energies of 434–588 keV. The coincidence timing resolution ($FWHM_{DET/DET}$) was acquired by correcting the contribution of the single timing resolution of the reference detector (STR_{REF}) from the FWHM of the Gaussian function fitted to the time difference histogram ($FWHM_{DET/REF}$) with the following equation:

$$FWHM_{DET/DET} = \sqrt{2} \times \sqrt{FWHM^2_{DET/REF} - STR^2_{REF}}$$

The timing resolution was obtained for each segment of each scintillator.

3. Results

3.1. Monte Carlo simulation

Using the GATE v.7.0 Monte Carlo simulation toolkit, we investigated the DOI-encoding capability of the proposed two-step DOI detector for six different detector configurations. When the crystal surface is treated with unpolished finish, optical photons are more likely to

disperse into adjacent crystals because diffused reflection occurs on the unpolished surface. As a result, the unpolished crystals with an air gap achieved very good DOI identification, as shown in figure 6(a). When optical adhesive was applied between unpolished crystals, each 9×9 crystal exhibited two well-separated peaks with the highest peak separation distance, as shown in figure 6(b). The use of optical adhesive with a similar refractive index as the scintillation crystal is expected to give better light dispersion in the crystals than with an air gap because the critical angle increases, thus yielding better DOI-encoding capability. In the case of polished single-layer crystals with air gaps, as shown in figure 6(c), the gamma-ray interaction positions in each crystal formed only one peak for the 9×9 scintillators, indicating no DOI-encoding capability. This was mainly because total reflection at the boundaries of the crystal surface and the air gap is highly probable in a polished crystal; hence, optical photons do not easily disperse through adjacent crystals. When using optical adhesive between polished crystals, more light spreads into the adjacent crystal owing to refractive index matching. As a result, we observed two segments of the DOI layer in the flood histogram, as shown in figure 6(d). The DOI detectors based on two-layer stacked polished crystals showed limited DOI separation if air gaps were used, as shown in figure 6(e). Figure 6(f) shows improved DOI separation using RTV gaps. The extent of the peak position shift was greater than in the detector based on single-layer polished scintillators and air gaps because of the high dispersion of scintillation photons at the boundary between the two layers.

3.2. Experimental data

3.2.1. DOI identification performance. The 2D gamma-ray interaction positions on the flood map were shifted towards the opposite direction from that of the surfaces covered by the stair-pattern reflectors, as shown in figures 7(a) and (b). Because of the depth-dependent offset of the reflector arrangements, the peak positions of the upper and lower segments shifted in opposite directions and the peaks could be separated, as shown in figure 7(c).

The flood histograms acquired using the DOI blocks with air gaps from the front-on irradiation scheme are shown in figures 8(a)–(c). Two-step DOI could be obtained from the flood maps of detectors ${}_{\mathrm{U}}\mathrm{S}_{\mathrm{Air}}$ and ${}_{\mathrm{P}}\mathrm{T}_{\mathrm{Air}}$ by assigning the DOI information to each gamma-ray event according to a peak position segmentation map, as shown in figure 8(d). The segmentation map was automatically derived from a flood map which was pre-processed with image filters (i.e. both Gaussian and Laplacian). Then the segmentation map was generated by finding each peak position and utilizing a minimum distance map of the peak positions. The ratio between the number of events classified to either segment was 1.2:1 (upper/lower segments). For detector ${}_{\mathrm{P}}\mathrm{S}_{\mathrm{Air}}$, the DOI could not be obtained from the flood map because of the limited shift of the peak position or scintillation photon transmission. The average distance between two peak positions in each scintillator (i.e. the distance between the peak position in the upper segment and that in the lower segment of the same scintillator) of detectors ${}_{\mathrm{U}}\mathrm{S}_{\mathrm{Air}}$, ${}_{\mathrm{P}}\mathrm{S}_{\mathrm{Air}}$ and ${}_{\mathrm{P}}\mathrm{T}_{\mathrm{Air}}$ was 10.63 ± 1.67, 5.99 ± 1.54, and 10.22 ± 1.58 pixels, respectively. Unlike the simulation result for detector ${}_{\mathrm{P}}\mathrm{S}_{\mathrm{Air}}$ in which no peak position shift was observed, the experimental study showed a peak position shift because of the non-ideal environment. Detector ${}_{\mathrm{P}}\mathrm{S}_{\mathrm{Air}}$ showed poorer results than the other two detectors because a limited number of scintillation photons were transported into adjacent scintillators. The average PVR and DWR of the central 3×3 scintillators were 2.09 ± 0.4 and 1.48 ± 0.16 for detector ${}_{\mathrm{U}}\mathrm{S}_{\mathrm{Air}}$ and 2.26 ± 0.78 and 1.55 ± 0.23 for detector ${}_{\mathrm{P}}\mathrm{T}_{\mathrm{Air}}$. Figures 8(e) and (f) show the 2D PVR and DWR histograms of the central 3×3 scintillators of detector ${}_{\mathrm{P}}\mathrm{T}_{\mathrm{Air}}$.

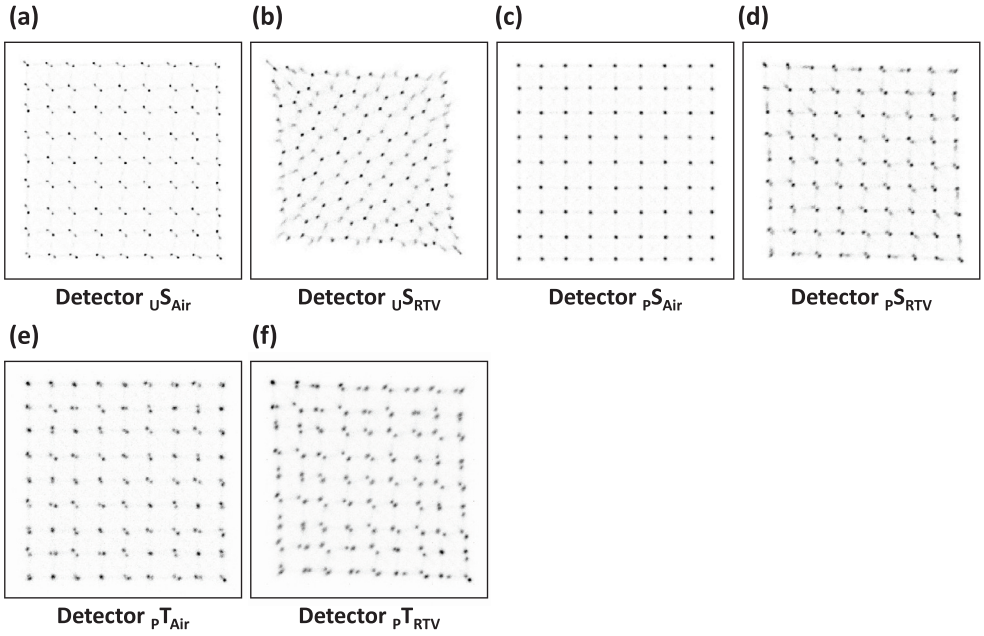

Figure 6. The Monte Carlo simulation results. The flood maps of the two-step DOI detectors based on (a) unpolished single-layer crystals with air gaps, (b) unpolished single-layer crystals with optical adhesive gaps, (c) polished single-layer crystals with air gaps, (d) polished single-layer crystals with optical adhesive gaps, (e) polished two-layer stacked crystals with air gaps, and (f) polished two-layer stacked crystals with optical adhesive gaps.

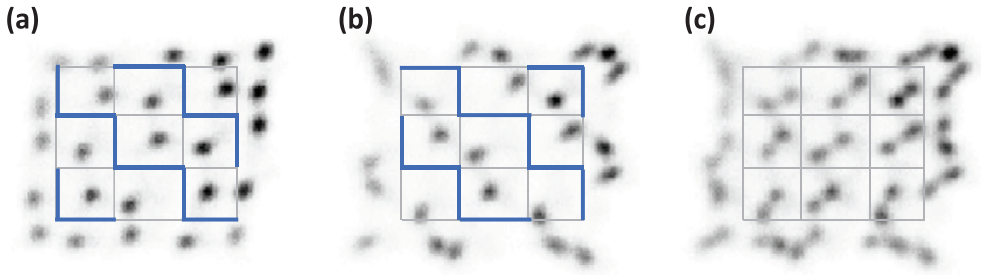

Figure 7. The flood maps of (a) the upper and (b) the lower segments of detector $_{U}S_{Air}$ acquired from the side-on irradiation scheme. The blue lines represent a stair-pattern reflector arrangement of the central 3 × 3 crystals in each segment. (c) The summed flood map of (a) and (b).

The flood histograms acquired from the DOI blocks with RTV silicone gaps are shown in figures 9(a)–(c). Two-step DOI could be obtained from the three detectors. Unlike detector $_{P}S_{Air}$, detector $_{P}S_{RTV}$ showed a separation of the peak positions because of the enhanced light transmission between adjacent scintillators induced by RTV silicone. The average distance between two peak positions in the scintillators of detectors $_{U}S_{RTV}$, $_{P}S_{RTV}$ and $_{P}T_{RTV}$ were 14.95 ± 2.80, 9.11 ± 1.90 and 11.28 ± 2.33 pixels, respectively. The average PVR and DWR of the central 3 × 3 scintillators were, correspondingly, 1.99 ± 0.43 and 1.65 ± 0.21

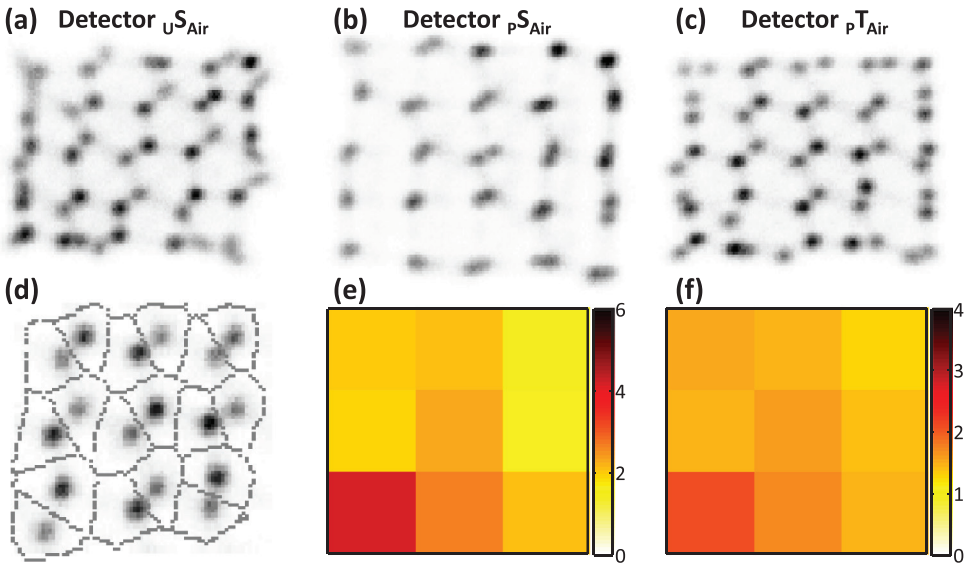

Figure 8. DOI identification performance of the detectors with air gaps. The flood maps acquired using (a) the unpolished single-layer crystal block ($_{U}S_{Air}$), (b) the polished single-layer crystal block ($_{P}S_{Air}$), and (c) the polished two-layer stacked crystal block ($_{P}T_{Air}$). (d) The segmentation map of the 2D peak positions of detector $_{P}T_{Air}$. The 2D histograms of (e) PVR and (f) DWR of the central 3 × 3 scintillators of detector $_{P}T_{Air}$.

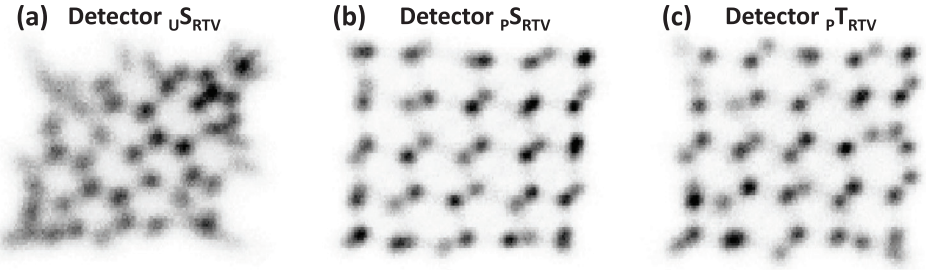

Figure 9. DOI identification performance of the detectors with RTV gaps. The flood maps acquired using (a) the unpolished single-layer crystal block ($_{U}S_{RTV}$), (b) the polished single-layer crystal block ($_{P}S_{RTV}$), and (c) the polished two-layer stacked crystal block ($_{P}T_{RTV}$).

for detector $_{U}S_{RTV}$, 1.65 ± 0.33 and 1.34 ± 0.15 for detector $_{P}S_{RTV}$, and 2.01 ± 0.87 and 1.45 ± 0.31 for detector $_{P}T_{RTV}$. The DOI identification performance is summarized in tables 2 and 3.

3.2.2. Energy performance. Among the detectors with air gaps, the lower layer of detector $_{P}T_{Air}$ showed the highest 511 keV peak. However, the photopeak position of the upper layer of the detector was 20% lower because of the loss of scintillation light at the boundaries of the two layers. Detector $_{U}S_{Air}$ showed the lowest 511 keV peak among the detectors with air gaps because unpolished scintillators have a higher photon escape probability and thus higher photon attenuation than polished scintillators. The photopeak of detector $_{P}S_{Air}$ was observed between those of the other two detectors, at a position similar to or slightly lower than that of detector

Table 2. DOI identification accuracies of the DOI detectors with air gaps: mean ± standard deviation (best, worst).

Parameter	Detector $_{U}S_{Air}$	Detector $_{P}S_{Air}$	Detector $_{P}T_{Air}$
PVR	2.09 ± 0.45 (2.75, 1.30)	N/A	2.26 ± 0.78 (4.14, 1.64)
DWR	1.48 ± 0.16 (1.68, 1.20)	N/A	1.55 ± 0.23 (2.08, 1.26)
Peak distance (pixel)	10.63 ± 1.67 (12.70, 7.58)	5.99 ± 1.54[a] (8.54, 3.61)	10.22 ± 1.58 (13.48, 8.44)
DOI accuracy (%)	95.67 ± 1.86 (97.61, 92.22)	N/A	96.17 ± 1.74 (99.27, 93.06)

[a]Measured from side-on irradiation data.
N/A, not applicable.

Table 3. DOI identification accuracies of the DOI detectors with RTV silicone gaps: mean ± standard deviation (best, worst).

Parameter	Detector $_{U}S_{RTV}$	Detector $_{P}S_{RTV}$	Detector $_{P}T_{RTV}$
PVR	1.99 ± 0.43 (2.45, 1.29)	1.65 ± 0.33[a] (2.23, 1.32)	2.01 ± 0.87[a] (3.56, 1.10)
DWR	1.65 ± 0.21 (1.90, 1.26)	1.34 ± 0.15[a] (1.50, 1.22)	1.45 ± 0.31[a] (2.01, 1.12)
Peak distance (pixel)	14.95 ± 2.80 (18.2, 8.9)	9.11 ± 1.90 (11.4, 5.36)	11.28 ± 2.33 (14.82, 8.93)
DOI accuracy (%)	97.02 ± 1.82 (98.75, 93.19)	94.79 ± 3.05[a] (99.11, 90.66)	94.06 ± 1.90[a] (97.06, 91.47)

[a]The result of one scintillator was excluded in which the two peak positions were very close.

REF. Similar energy resolutions, from 9.1% to 10.6%, were obtained for detectors $_{P}S_{Air}$, $_{P}T_{Air}$ and REF. For detector $_{U}S_{Air}$, the energy resolution was degraded—especially in the lower segment, where it was 16.6%—mainly because of the depth-dependent photopeak difference.

Regarding the detectors with RTV silicone gaps, detector $_{P}S_{RTV}$ showed the highest 511 keV peak, followed by detector $_{P}T_{RTV}$ and $_{U}S_{RTV}$. The detectors exhibited lower photopeak positions and degraded energy resolutions compared with those with air gaps because of the light attenuation in RTV silicone. The energy resolutions of detectors $_{P}S_{RTV}$ and $_{P}T_{RTV}$ were 12.9–13.3%. Detector $_{U}S_{RTV}$ had an average energy resolution of 21.9%. These results are summarized in tables 4 and 5.

Representative energy spectra of an arbitrarily selected scintillator in each DOI detector are shown in figure 10.

3.2.3. Timing performance. Among the detectors with air gaps, the DOI arrays based on polished scintillators showed similar coincidence timing resolution, approximately 420 ps in detector $_{P}S_{Air}$ and the lower layer of detector $_{P}T_{Air}$. The upper layer of detector $_{P}T_{Air}$ had a degraded timing resolution of 453 ps because of the higher light loss and photon path length variation. Detector $_{U}S_{Air}$ also exhibited a degraded timing resolution of approximately 465 ps because of the lower 511 keV peak and inferior energy resolution compared with the other detectors. The average timing resolution of detector REF was approximately 395 ps.

The detectors with RTV silicone gaps showed degraded timing resolutions compared with the detectors with air gaps because of the photon attenuation in RTV silicone. The average timing resolution of detectors $_{P}S_{RTV}$ and $_{P}T_{RTV}$ was approximately 477 ps and that of detector $_{U}S_{RTV}$ was approximately 569 ps. The results are summarized in tables 4 and 5.

Table 4. Energy and time performance of the DOI detectors with air gaps.

	Detector $_{U}S_{Air}$		Detector $_{P}S_{Air}$		Detector $_{P}T_{Air}$		Detector REF	
Parameter	Upper	Lower	Upper	Lower	Upper	Lower	Upper	Lower
511 keV peak position (a.u.)	79.0	88.5	91.2	90.7	81.3	100	89.8	94.3
Energy resolution (FWHM) (%)	11.1 ± 0.4	16.6 ± 0.6	9.4 ± 0.3	9.4 ± 0.2	9.4 ± 0.4	10.6 ± 0.2	9.1 ± 0.3	10.1 ± 0.5
Timing resolution (FWHM) (ps)	438 ± 10	491 ± 10	407 ± 11	432 ± 11	453 ± 19	420 ± 12	371 ± 11	408 ± 7

Table 5. Energy and time performance of the DOI detectors with RTV silicone gaps.

	Detector $_{U}S_{RTV}$		Detector $_{P}S_{RTV}$		Detector $_{P}T_{RTV}$	
Parameter	Upper	Lower	Upper	Lower	Upper	Lower
511 keV peak position (a.u.)	48.0	56.8	82.9	85.7	70.4	72.9
Energy resolution (FWHM) (%)	18.0 ± 4.9	25.7 ± 3.5	13.0 ± 1.2	13.3 ± 0.8	12.9 ± 1.2	13.1 ± 0.9
Timing resolution (FWHM) (ps)	572 ± 39	565 ± 37	451 ± 35	479 ± 26	476 ± 33	500 ± 41

The 2D histograms of coincidence resolving times of the detectors containing the scintillator with the best and the worst timing resolution are shown in figure 11 with the distributions of time differences. In the distributions, left tails appeared because energy cutoff of the reference detector was not done due to the limitation of the acquisition setup of the reference detector and scattered events were not removed. The effect of degradation of timing resolution due to the tail was corrected when calculating the coincidence resolving time of the DOI detector using the equation shown in section 2.4.3.

4. Discussion

Using the proposed design, DOI information can be obtained without adding resources (i.e. additional photosensors or data acquisition systems) or increasing the processing time (i.e. for acquiring training sets or applying estimation algorithms). In this novel DOI detector, we used six different detector configurations to investigate and evaluate the detector performance, including the DOI identification accuracy and the energy and time performance. Good DOI identification accuracies were obtained in all detectors except $_{P}S_{Air}$. The time performance of detector $_{P}T_{Air}$ was degraded by only approximately 40 ps relative to that of detector REF because of the higher light loss and increased path length variation; this degradation was a trade-off for obtaining two-step DOI information. Because detector $_{P}T_{Air}$ showed the best energy and timing performance, its configuration can be adopted in PET detectors with fine time performance for constructing TOF-DOI PET systems. In contrast, when manufacturing cost is more important than energy and timing performance, the configurations of detectors $_{U}S_{Air}$ and $_{P}S_{RTV}$ are favorable because they require no additional cutting of the scintillators. Furthermore, detectors $_{U}S_{Air}$ and $_{P}S_{RTV}$ do not require an alignment of the upper and lower layers.

The image quality of DOI PET relies heavily on the PCE on the flood map. The methods based on pulse shape analysis or dual-ended readout (e.g. Delfino *et al* 2010, Kang *et al* 2015)

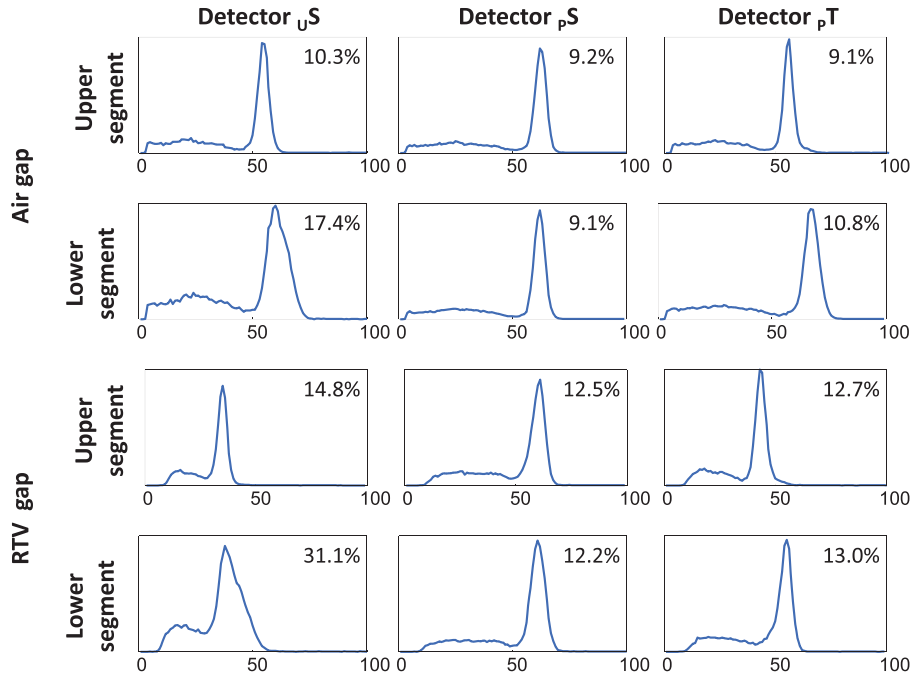

Figure 10. Representative energy spectra and resolution of one arbitrarily selected scintillator from each DOI detector.

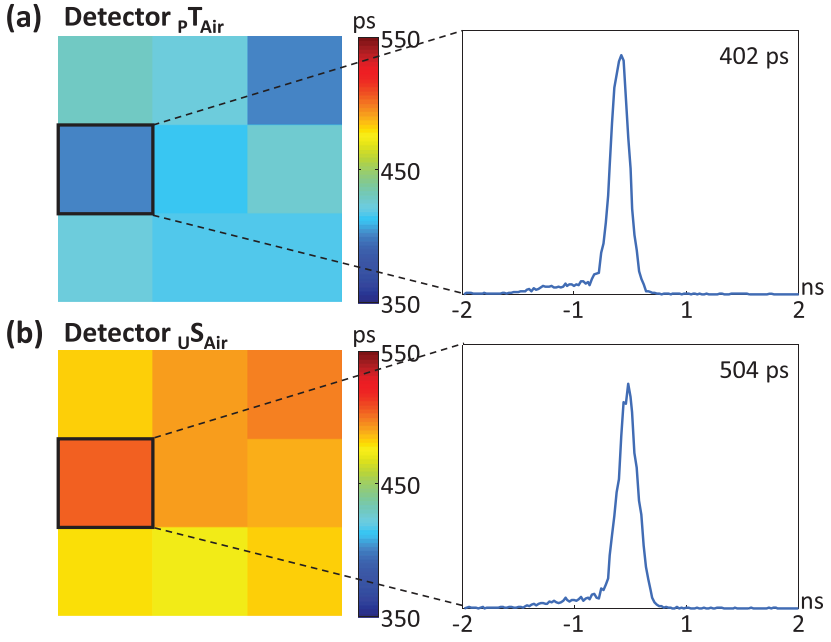

Figure 11. Representative 2D histograms of coincidence-resolving times and distributions of time differences obtained by using (a) detector $_P$T$_{Air}$ (the best timing resolution) and (b) detector $_U$S$_{Air}$ (the worst timing resolution).

Table 6. Summary of energy and timing performance (average of upper and lower segments).

Parameter	Detector $_{U}S_{Air}$	Detector $_{U}S_{RTV}$	Detector $_{P}S_{Air}$	Detector $_{P}S_{RTV}$	Detector $_{P}T_{Air}$	Detector $_{P}T_{RTV}$	Detector REF
511 keV peak position (a.u.)	83.8	52.4	91.0	84.3	90.3	71.7	92.1
Energy resolution (FWHM) (%)	13.9	21.9	9.4	13.2	10.0	13.0	9.6
Timing resolution (FWHM) (ps)	465	569	420	465	437	488	390

have equivalent PCE to non-DOI detectors. The PCE of continuous crystal approaches (Ling *et al* 2007, Maas *et al* 2009, Chung *et al* 2010) depends on the crystal thickness, surface treatment condition and position/DOI estimation methods. In the DOI encoding methods based on the different reflector arrangements and DOI-dependent peak position shift (the current proposed method; Murayama *et al* 1998, Tsuda *et al* 2004, Inadama *et al* 2008, Düppenbecker *et al* 2011, Hunter *et al* 2015, Pizzichemi *et al* 2016) the PCE depends on the extent and direction of peak separation and peak position uncertainty. In this study, we measured several qualitative and quantitative PCE parameters, but it should be noted that these parameters also depend on the crystal pixel size and photodetector granularity (e.g. the size of PMT anode).

Ideally, the suggested two-step DOI detectors can attain the largest peak position distance on the flood map because they can provide uniformly distributed or evenly spaced peak positions in flood maps with a pitch of $d/\sqrt{2}$ pitch, where d is the original crystal pitch of a non-DOI detector. However, both the simulations and the experiments obtained non-ideal flood maps with unevenly distributed peak positions. The main reason for this is the opposite directions between the peak position shifts of the upper and lower segments (e.g. upward and rightward directions in the upper segment and downward and leftward directions at the lower segment). During their propagation to the entrance window of a photosensor, some scintillation photons are reflected by the other segment to the opposite direction to the original one, thus reducing the shift of the peak position. As shown in figure 7(a), this effect is enhanced for interactions occurring in the upper segment (i.e. far from the PMT window) because, unlike the case of the lower segment, where approximately half of the photons propagate to the other segment and reach the photosensor window, every photon generated from the upper segment passes through the lower segment, thus increasing the probability of reflection in the opposite direction. SiPMs with fine pixel size and pitch can also be used as photosensors in the proposed DOI detectors. It is expected that SiPM-based light readout yields better outcome because of the reduced light dispersion between scintillator and photosensor (in the Hamamatsu H9500 PMT the 1.5 mm entrance window above the photocathode causes considerable light dispersion).

Several studies have proposed DOI PET detectors that obtain DOI information using flood histograms based on depth-dependent peak position shifts (Tsuda *et al* 2004, Inadama *et al* 2008, Ito *et al* 2010a, Chung *et al* 2011). In two-step DOI detectors, the largest peak-position distance on the flood map can be achieved only by using the construction methods proposed in Ito *et al* (2010a) and in this study. The comparison of the two designs suggests that the method proposed in Ito *et al* (2010a) provides better DOI identification accuracy because it is not affected by conflicting directions of peak position shift between the two segments, as discussed earlier. However, the method proposed in this study has an advantage in terms of simplicity because it requires less time and effort for the precise alignment of the upper and lower segments if detectors $_{U}S_{Air}$ or $_{P}S_{RTV}$ were used.

A limitation of the proposed design is the difficulty in separating the peak positions of the scintillators in the edge regions and, therefore, in obtaining accurate DOI information. This is because the outer surfaces of the edge scintillators in both segments are covered by reflectors, thus reducing the achievable distance between two peak positions. This problem can be mitigated by maintaining the stair-shaped reflector arrangement at the outermost sides of the edge scintillators, which entails a compromise between DOI information and energy and time performance. An additional option is placing light guides on the sides of the edge crystals to enhance the scintillation photon transport outward from the crystals, thus increasing the distance between two peak positions. However, this solution is only possible when the entrance window of a photosensor not contacting the scintillators has space available for the positioning of light guides.

5. Summary and conclusions

We proposed a novel DOI PET detector design using a stair-shaped reflector arrangement and demonstrated the feasibility of two-step DOI detectors through simulations and experiments. The detector ${}_{\mathrm{P}}\mathrm{T}_{\mathrm{Air}}$ showed the best energy and timing performance, and thus its configuration can be adopted in PET detectors with fine time performance for constructing TOF-DOI PET systems. The detectors ${}_{\mathrm{U}}\mathrm{S}_{\mathrm{Air}}$ and ${}_{\mathrm{P}}\mathrm{S}_{\mathrm{RTV}}$ showed good DOI identification performance by using only single-layer scintillators, making them favorable when manufacturing cost is more important than timing performance. Therefore, the proposed method is a promising candidate for PET scanners that require high resolution and sensitivity and operate with conventional acquisition systems.

Acknowledgments

This work was supported by grants from the National Research Foundation of Korea (NRF), which is funded by the Korean Ministry of Science, ICT and Future Planning (grant nos NRF-2014M3C7034000 and NRF-2016R1A2B3014645).

References

Berg E, Roncali E, Kapusta M, Du J and Cherry S R 2016 A combined time-of-flight and depth-of-interaction detector for total-body positron emission tomography *Med. Phys.* **43** 939–50

Cates J W and Levin C S 2016 Advances in coincidence time resolution for PET *Phys. Med. Biol.* **61** 2255–64

Chung Y H, Baek C-H, Lee S-J, Hong K J, Kang J H and Choi Y 2010 Preliminary experimental results of a quasi-monolithic detector with DOI capability for a small animal PET *Nucl. Instrum. Methods* A **621** 590–4

Chung Y H, Hwang J Y, Baek C-H, Lee S-J, Ito M, Lee J S and Hong S J 2011 Monte Carlo simulation of a four-layer DOI detector with relative offset in animal PET *Nucl. Instrum. Methods* A **626–7** 11–21

Delfino E P, Majewski S, Raylman R R and Stolin A 2010 Towards 1 mm PET resolution using DOI modules based on dual-sided SiPM readout *NSS/MIC: IEEE Nuclear Science Symp. Conf. Record (Knoxville, 2010)* pp 3442–9

Dokhale P A, Silverman R W, Shah K S, Grazioso R, Farrell R, Glodo J, McClish M A, Entine G, Tran V-H and Cherry S R 2004 Performance measurement of a depth-encoding PET detector module based on position-sensitive avalanche photodiode read-out *Phys. Med. Biol.* **49** 4293–304

Düpenbecker P M, Lodomez S, Haagen R, Marsden P K and Schulz V 2011 Investigation of a sub-millimeter resolution PET detector with depth of interaction encoding using digital SiPM single sided readout *NSS/MIC: IEEE Nuclear Science Symp. Conf. Record (Valencia, 2011)* pp 2252–3

Hunter W C J, Miyaoka R S, MacDonald L, McDougald W and Lewellen T K 2015 Light-sharing interface for dMiCE detectors using sub-surface laser engraving *IEEE Trans. Nucl. Sci.* **62** 27–35
Inadama N, Murayama H, Yamaya T, Nishikido F, Shibuya K, Yoshida E, Tsuda T, Omura A, Yazaki Y and Osada H 2008 DOI PET detectors with scintillation crystals cut as triangular prisms *NSS/MIC: IEEE Nuclear Science Symp. Conf. Record (Dresden, 2008)* pp 3942–5
Ito M, Lee J S, Kwon S I, Lee G S, Hong B, Lee K S, Sim K-S, Lee S J, Rhee J T and Hong S J 2010a A four-layer DOI detector with a relative offset for use in an animal PET system *IEEE Trans. Nucl. Sci.* **57** 976–81
Ito M, Lee J S, Park M-J, Sim K-S and Hong S J 2010b Design and simulation of a novel method for determining depth-of-interaction in a PET scintillation crystal array using a single-ended readout by a multi-anode PMT *Phys. Med. Biol.* **55** 3827–41
Ito M, Hong S J and Lee J S 2011 Positron emission tomography (PET) detectors with depth-of-interaction (DOI) capability *Biomed. Eng. Lett.* **1** 70–81
Ito M, Lee M S and Lee J S 2013 Continuous depth-of-interaction measurement in a single-layer pixelated crystal array using a single-ended readout *Phys. Med. Biol.* **58** 1269–82
Jan S *et al* 2004 GATE: a simulation toolkit for PET and SPECT *Phys. Med. Biol.* **49** 4543–61
Kang H G, Ko G B, Rhee J T, Kim K M, Lee J S and Hong S J 2015 A dual-ended readout detector using a meantime method for SiPM TOF-DOI PET *IEEE Trans. Nucl. Sci.* **62** 1935–43
Karp J S, Surti S, Daube-Witherspoon M E, Freifelder R, Cardi C A, Adam L-E, Bilger K and Muehllehner G 2003 Performance of a brain PET camera based on Anger-logic gadolinium oxyorthosilicate detectors *J. Nucl. Med.* **44** 1340–9
Ko G B and Lee J S 2015 Performance characterization of high quantum efficiency metal package photomultiplier tubes for time-of-flight and high-resolution PET applications *Med. Phys.* **42** 510–20
Ko G B, Kim K Y, Yoon H S, Lee M S, Son J-W, Im H-J and Lee J S 2016 Evaluation of a silicon photomultiplier PET insert for simultaneous PET and MR imaging *Med. Phys.* **43** 72–83
Kwon S I, Hong S J, Ito M, Yoon H S, Lee G S, Sim K-S, Rhee J T, Lee D S and Lee J S 2008 Development of position encoding circuit for a multi-anode position sensitive photomultiplier tube *Nucl. Med. Mol. Imaging* **42** 469–77
Kwon S I and Lee J S 2014 Signal encoding method for a time-of-flight PET detector using a silicon photomultiplier array *Nucl. Instrum. Methods* A **761** 39–45
Kwon S I, Lee J S, Yoon H S, Ito M, Ko G B, Choi J Y, Lee S-H, Song I C, Jeong J M, Lee D S and Hong S J 2011 Development of small-animal PET prototype using silicon photomultiplier (SiPM): initial results of phantom and animal imaging studies *J. Nucl. Med.* **52** 572–80
Lee C M, Kwon S I, Ko G B, Ito M, Yoon H S, Lee D S, Hong S J and Lee J S 2012 A novel compensation method for the anode gain non-uniformity of multi-anode photomultiplier tubes *Phys. Med. Biol.* **57** 191–207
Lee I, Paeng J C, Lee S J, Shin C S, Jang J-Y, Cheon G J, Lee D S, Chung J-K and Kang K W 2015 Comparison of diagnostic sensitivity and quantitative indices between ^{68}Ga-DOTATOC PET/CT and ^{111}In-pentetreotide SPECT/CT in neuroendocrine tumors: a preliminary report *Nucl. Med. Mol. Imaging* **49** 284–90
Lee M S and Lee J S 2015 Depth-of-interaction measurement in a single-layer crystal array with a single-ended readout using digital silicon photomultiplier *Phys. Med. Biol.* **60** 6495–514
Lee S-H and Park H 2014 Parametric response mapping of longitudinal PET scans and their use in detecting changes in Alzheimer's diseases *Biomed. Eng. Lett.* **4** 73–9
Levin A and Moisan C 1996 A more physical approach to model the surface treatment of scintillation counters and its implementation into DETECT *NSS/MIC: IEEE Nuclear Science Symp. Conf. Record (Anaheim, 1996)* pp 702–6
Ling T, Lewellen T K and Miyaoka R S 2007 Depth of interaction decoding of a continuous crystal detector module *Phys. Med. Biol.* **52** 2213–28
Liu H, Omura T, Watanabe M, Yamashita T 2001 Development of a depth of interaction detector for gamma-rays *Nucl. Instrum. Methods* A **459** 182–90
Maas M C, Schaart D R, van der Laan D J, Bruyndonckx P, Lemaître C, Beekman F J and van Eijk C W E 2009 Monolithic scintillator PET detectors with intrinsic depth-of-interaction correction *Phys. Med. Biol.* **54** 1893–908
Marcinkowski R, España S, Holen R V and Vandenberghe S 2014 Optimized light sharing for high-resolution TOF PET detector based on digital silicon photomultipliers *Phys. Med. Biol.* **59** 7125–39
Murayama H, Ishibashi H, Uchida H, Omura T and Yamashita T 1998 Depth encoding multicrystal detectors for PET *IEEE Trans. Nucl. Sci.* **45** 1152–7

Nishikido F, Inadama N, Yoshida E, Murayama H and Yamaya T 2014 Optimization of the refractive index of a gap material used for the 4-layer DOI detector *IEEE Trans. Nucl. Sci.* **61** 1066–73

Pizzichemi M, Stringhini G, Niknejad T, Liu Z, Lecoq P, Tavernier S, Varela J, Paganoni M and Auffray E 2016 A new method for depth of interaction determination in PET detectors *Phys. Med. Biol.* **61** 4679–98

Schellenberg G, Stortz G and Goertzen A L 2016 An algorithm for automatic crystal identification in pixelated scintillation detectors using thin plate splines and Gaussian mixture models *Phys. Med. Biol.* **61** N90–101

Seidel J, Vaquero J J, Siegel S, Gandler W R and Green M V 1999 Depth identification accuracy of a three layer phoswich PET detector module *IEEE Trans. Nucl. Sci.* **46** 485–90

Siegel S, Silverman R W, Shao Y and Cherry S R 1996 Simple charge division readouts for imaging scintillator arrays using a multi-channel PMT *IEEE Trans. Nucl. Sci.* **43** 1634–41

Son J-W, Ko G B, Won J Y, Yoon H S and Lee J S 2016 Development and performance evaluation of a time-of-flight positron emission tomography detector based on a high-quantum-efficiency multi-anode photomultiplier tube *IEEE Trans. Nucl. Sci.* **63** 44–51

Spanoudaki V C and Levin C S 2011 Investigating the temporal resolution limits of scintillation detection from pixellated elements: comparison between experiment and simulation *Phys. Med. Biol.* **56** 735–56

Stonger K A and Johnson M T 2004 Optimal calibration of PET crystal position maps using Gaussian mixture models *IEEE Trans. Nucl. Sci.* **51** 85–90

Streun M *et al* 2014 PhenoPET: a dedicated PET scanner for plant research based on digital SiPMs (DPCs) *NSS/MIC: IEEE Nuclear Science Symp. Conf. Record (Seattle, 2014)* pp 1–3

Tashima H *et al* 2016 Development of a small single-ring OpenPET prototype with a novel transformable architecture *Phys. Med. Biol.* **61** 1795–809

Troost E G C, Bussink J, Hoffmann A L, Boerman O C, Oyen W J G and Kaanders J H A M 2010 ^{18}F-FLT PET/CT for early response monitoring and dose escalation in oropharyngeal tumors *J. Nucl. Med.* **51** 866–74

Tsuda T, Murayama H, Kitamura K, Yamaya T, Yoshida E, Omura T, Kawai H, Inadama N and Orita N 2004 A four-layer depth of interaction detector block for small animal PET *IEEE Trans. Nucl. Sci.* **51** 2537–42

Won J Y, Kwon S I, Yoon H S, Ko G B, Son J-W and Lee J S 2016 Dual-phase tapped-delay-line time-to-digital converter with on-the-fly calibration implemented in 40 nm FPGA *IEEE Trans. Biomed. Circuits Syst.* **10** 231–42

Wong W-H, Li H, Zhang Y, Ramirez R, An S, Wang C, Liu S, Dong Y and Baghaei H 2015 A high-resolution time-of-flight clinical PET detection system using a gapless PMT-quadrant-sharing method *IEEE Trans. Nucl. Sci.* **62** 2067–74

Yamamoto S, Watabe H, Kanai Y, Watabe T, Kato K and Hatazawa J 2013 Development of an ultrahigh resolution Si-PM based PET system for animals *Phys. Med. Biol.* **58** 7875–88

Yamaya T, Hagiwara N, Obi T, Tsuda T, Kitamura K, Hasegawa T, Haneishi H, Inadama N, Yoshida E and Murayama H 2006 Preliminary resolution performance of the prototype system for a 4-layer DOI-PET scanner: jPET-D4 *IEEE Trans. Nucl. Sci.* **53** 1123–8

Yoo M Y, Paeng J C, Cheon G J, Lee D S, Chung J-K, Kim E E and Kang K W 2015 Prognostic value of metabolic tumor volume on ^{11}C-methionine PET in predicting progression-free survival in high-grade glioma *Nucl. Med. Mol. Imaging* **49** 291–7

Yoon H S, Ko G B, Kwon S I, Lee C M, Ito M, Song I C, Lee D S, Hong S J and Lee J S 2012 Initial results of simultaneous PET/MRI experiments with an MRI-compatible silicon photomultiplier PET scanner *J. Nucl. Med.* **53** 608–14

Yoon H S 2016 Network based high performance data acquisition system for PET scanner *PhD Thesis* Seoul National University, Seoul

Yu Y, Wang S, Wang X, Xia Y, Shang H, Wu J, Wang Q, Liu Y and Ma T 2014 Impact of depth-of-interaction on image resolution in long axial-FOV PET *NSS/MIC: IEEE Nuclear Science Symp. Conf. Record (Seattle, 2014)* pp 10–3

Zhang N, Thompson C J, Togane D, Cayouette F and Nguyen K Q 2002 Anode position and last dynode timing circuits for dual-layer BGO scintillator with PS-PMT based modular PET detectors *IEEE Trans. Nucl. Sci.* **49** 2203–7